




A comprehensive study on crystal structure, magnetic, and electrical properties of Ni-doped Fe–Cd spinel nano-ferrites

M. H. Nasr^{1,2,*}, M. M. Elkholy^{2,3}, L. M. S. El-Deen^{2,3}, A. S. Abouhaswa^{2,4,*} , Gamal M. Turky⁵, and A. A. EL-Hamalawy²

¹Department of Renewable Energy, Faculty of Technological Industry and Energy, Delta Technological University, Qeisna, Egypt

²Laboratory of Materials and Energy, Department of Physics, Faculty of Science, Menoufia University, 32511 Shebin El-Koom, Egypt

³Physics Department, Faculty of Science, New Mansoura University, Dakahlia, Egypt

⁴Institute of Natural Science and Mathematics, Ural Federal University, Ekaterinburg, Russia 620002

⁵Department of Microwave Physics & Dielectrics, National Research Centre, 12622 Giza, Egypt

Received: 21 January 2022

Accepted: 24 May 2022

Published online:

7 June 2022

© The Author(s), under exclusive licence to Springer Science+Business Media, LLC, part of Springer Nature 2022

ABSTRACT

The flash auto-combustion method was used to synthesize nanocrystalline spinel ferrites with the general formula $\text{Cd}_{1-x}\text{Ni}_x\text{Fe}_2\text{O}_4$ ($x = 0, 0.25, 0.50, 0.75, \text{ and } 1.0$). Structural characterizations of all prepared samples were carried out by the X-ray diffraction technique (XRD), Fourier transformation infrared spectroscopy (FTIR), and scanning electron microscope (SEM). Broadband dielectric spectroscopy (BDS) and vibration sample magnetometer (VSM) measurements were used to evaluate the dielectric and magnetic characteristics of the synthesized ferrite samples, respectively. The formation of the main cubic phase with space group Fd3m was confirmed by X-ray diffraction examination besides hematite hexagonal phase $\alpha\text{-Fe}_2\text{O}_3$. Rietveld refinement revealed that increasing Ni-doping content led to decrease the volume fraction of hematite hexagonal phase until it vanished at $x = 1$ and decreasing of lattice parameters. Along with the X-ray diffraction revealed that the particle size and lattice strain were increased with increasing Ni content (x). The two distinctive absorption bands of spinel ferrites were identified using FTIR, and their dependency on Ni concentration was studied and explained. The saturation magnetization (M_s) and coercivity (H_c) increased as the Ni concentration increased, according to VSM measurements. The frequency dependence of the permittivity for the studied composition as sintered @ 950 °C in comparison with the as-prepared ones shows development of a net of micro-capacitors like behavior in the former. This is due to a thin layer of weakly conducting grain boundaries separating the effectively conducting grains. The conductivity spectra of the compositions show two distinguished trends separated by a characteristic frequency. These three phenomena will be discussed and explained in some detail.

Address correspondence to E-mail: manasr10@hotmail.com; aliabohaswa@hotmail.com

1 Introduction

Recently, nano-sized spinel ferrites have been given significant attention due to their multilateral fundamental and technical applications, including ferrofluids, transducers, magnetic recorders, electromagnetic wave absorbers, drug delivery, magnetic resonance imaging, magnetic fluids, etc. [1]. Ferrites are magnetic materials having a variety of electrical and magnetic characteristics that may be employed in a variety of industrial and biological applications [2]. Spinel ferrites are preferred over other magnetic materials owing to their low eddy current losses, low coercivity, and high saturation magnetization. The typical formula for spinel ferrites is MFe_2O_4 , where Fe is iron and M is a divalent metal ion such as Cd, Ni, Mn, Co, and so on [3–7].

Spinel ferrites have Fd3m space group, which reveal face-centered cubic (fcc) structure [8].

Soft ferrites properties might also be easily adjusted by the combination and suitable addition of divalent and trivalent cations in the spinel structure to improve their characteristics. So, the purpose is to choose one of these ferrites, i.e., cadmium, because it is a true amorphous solid with a regular spinel structure and is well known as a geometrically challenged system. It is also used with nickel since Ni ion that is a relaxing ion with an orbital magnetic moment, making it ideal for peak power in standing devices [9].

Researchers are interested in CdNiFeO nano-ferrites having a spinel structure because of their features such as high electrical resistivity, high magnetic permeability, high Curie temperature, and due to their applications in the microwave, such as circulators, isolators, phase shifters etc., [10–12]. Nickel cation substitution is frequently recommended as a way to improve the magnetic, hyperthermal, and relaxometric characteristics of spinel ferrite [13, 14]. Nath et al. have studied the magnetic orders in soft Ni–Cd ferrite [15]. They discovered that the integration and appropriate addition of divalent and trivalent cations in the spinel structure may effectively improve the characteristics of soft ferrites.

Nickel ferrites nanoparticles have been synthesized using variety methods: high-energy ball milling [16], co-precipitation [17–19], and sol–gel combustion [20, 21]. In this work, we prefer sol–gel combustion because of a cost-effective and simple process with a high production rate [22]. Exothermic and self-

sustaining redox reactions between metal nitrates (oxidizer) and an organic complexant (reducing agent) are coupled in a chemical sol–gel and combustion process [23].

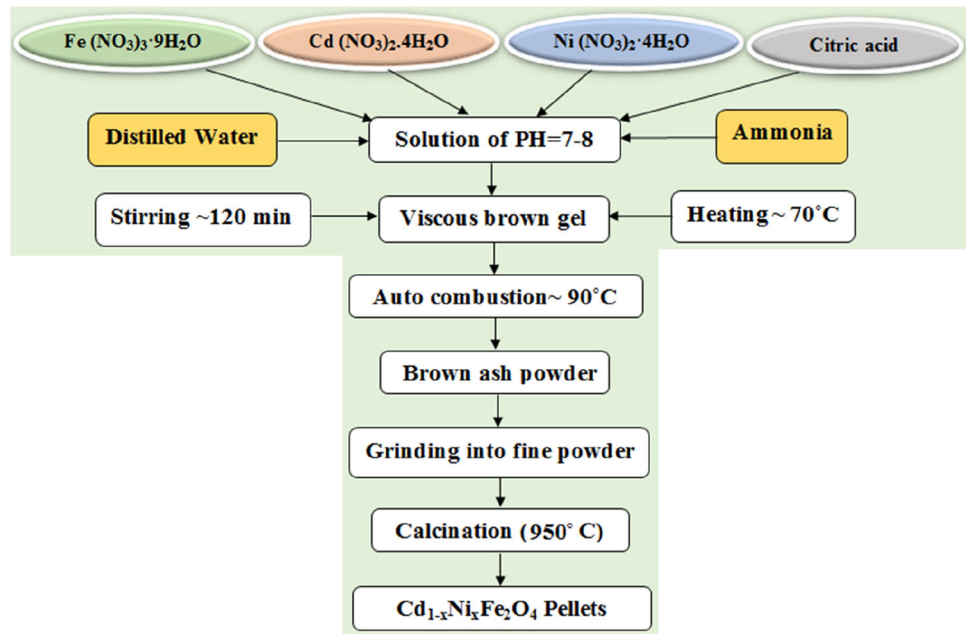
In the present work, an attempt to synthesis Cd–Ni spinel nano-ferrites with the general formula $Cd_{1-x}Ni_xFe_2O_4$ (in which $x = 0, 0.25, 0.5, 0.75, 1$) using a sol–gel combustion technique. The objective is to improve the structural, electrical, and magnetic characteristics of prepared $(Cd-Ni)F_2O_4$ spinel nano-ferrites by substituting Ni for Cd and to give a complete structural investigation of spinel ferrite nanoparticles with more precision characterization employing XRD, SEM, EDX, and FTIR. In addition, a broadband dielectric spectroscopy will be employed to consider the effect of Ni—substitution on the electrical conductivity and the dielectric behavior of the Cd—ferrite over a wide range of frequency and at ambient temperature.

2 Experimental technique

2.1 Materials and samples preparation

Spinel ferrite $Cd_{1-x}Ni_xFe_2O_4$ nanoparticle samples of different Ni ratios (x ranging between 0 and 1) were formed using a flash auto-combustion technique. Ferric nitrate $Fe(NO_3)_3 \cdot 9H_2O$ (99%) (LOBA CHEMIE), Cadmium nitrate $Cd(NO_3)_2 \cdot 6H_2O$ (99%) (LOBA CHEMIE), nickel nitrate $Ni(NO_3)_2 \cdot 4H_2O$ (99%) (CHEM-LAB), and citric acid ($C_6H_8O_7$, 99%) (LOBA CHEMIE) as starting chemicals were utilized. Figure 1 shows the flow chart for preparing steps in details through the combination of sol–gel and combustion techniques [24]. Small amounts of distilled water were used to dissolve stoichiometric quantities of the mentioned nitrates at room temperature, and citric acid was employed as a fuel. To ensure homogeneity, the resulting solution was mixed with a hotplate magnetic stirrer at 70 °C, and ammonia was used to fine tune the pH value. The mixture was heated at about 95 °C with constant stirring to remove any remaining water. The brown gel was spontaneously ignited in the presence of ambient air, resulting in the formation of light brown ash powder. The porous ash samples were crushed into a fine powder and annealed at 950 °C.

Fig. 1 Flow chart for preparing samples steps of $\text{Cd}_{1-x}\text{Ni}_x\text{Fe}_2\text{O}_4$ spinel ferrite nanoparticle



2.2 Samples characterization

2.3 X-ray diffraction, SEM and FTIR

At room temperature, X-ray diffraction measurements were used to examine the structure of the samples and phase purity using a Bruker D8 Advance diffractometer with $\text{CuK}\alpha$ radiation ($\lambda = 1.5418 \text{ \AA}$). The diffraction data were collected for 2θ values ranging between 2° and 70° with scanning speed of $2^\circ/\text{min}$. The images for the examined samples were produced using a scanning electron microscope model Quanta 250 FEG (Field Emission Gun) connected to an EDX unit (Energy Dispersive X-ray Analyses) with a 30 kV accelerating voltage, magnification range of 14 to 1,000,000, and resolution of Gun.1n. Fourier transform infrared spectroscopy (FTIR) spectra for all examined samples were studied by using infrared spectrometer Perkin-Elmer 1430, Germany in the $200\text{--}4000 \text{ cm}^{-1}$ wavenumber range.

2.4 Magnetic investigations

The vibrating sample magnetometer (VSM) was used to explore magnetic hysteresis characteristics in magnetic fields with intensities up to 25 kOe at room temperature.

2.5 Electrical and dielectric properties

The electrical conductivity and dielectric properties of the investigated samples were measured in the frequency range 0.1 Hz to 10 MHz, using broadband dielectric spectroscopy (BDS). This spectroscopy utilizing a high-resolution Alpha analyzer with an active sample head (Novocontrol GmbH- concept 40). The samples' powders were compacted into pellets of 12 mm diameter and about 1 mm thickness.

In parallel plate geometry, the disk was sandwiched between two gold-plated brass electrodes. The real, ϵ' and imaginary, ϵ'' , parts of the complex permittivity will be determined for all the investigated samples. The complex dielectrics function: $\epsilon^*(f) = \epsilon'(f) - i\epsilon''(f)$ where ϵ' is the permittivity and ϵ'' is the dielectric loss. It is equivalent with the complex conductivity function: $\sigma^*(f) = \sigma'(f) + i\sigma''(f)$ since $\sigma^*(f) = if\epsilon_0\epsilon^*(f)$, implying that $\sigma'(f) = f\epsilon_0\epsilon''(f)$ and $\sigma'' = f\epsilon_0\epsilon'$ (ϵ_0 being the vacuum permittivity and f is the frequency).

3 Results and discussion

3.1 X-ray diffraction

X-ray diffraction (XRD) patterns of the prepared spinel ferrite system $\text{Cd}_{1-x}\text{Ni}_x\text{Fe}_2\text{O}_4$ ($x = 0.0, 0.25, 0.5, 0.75, 1.0$) sintered at 950°C are presented in Fig. 2. As

is obvious from the figure, the XRD revealed the existence of cubic phase spinel ferrite with space group $Fd\bar{3}m$. The main peaks could be indexed as (220), (311), (400), (422), (511), and (440) are major lattice planes, which of the cubic spinel structure's characteristics. Moreover, we noticed the appearance of second phase except the sample ($x = 1$), the second phase contains the peaks of the hematite hexagonal phase $\alpha\text{-Fe}_2\text{O}_3$ (JCPDS#86-0550) with space group $R\text{-}3c$ with lattice parameter $a = b = 5.03 \text{ \AA}$, $c = 13.73 \text{ \AA}$. The formation of the hematite hexagonal phase $\alpha\text{-Fe}_2\text{O}_3$ was caused by inadequate Cd ion diffusion into the ferrite matrix [25]. The inset in Fig. 1 illustrates the remarkable shift of the main peak (311) for cubic phase spinel ferrite in the direction of higher degree (2θ) with the increase in nickel substitution ratio. This can be accredited to larger ionic radius of cadmium (0.97 \AA) than that of nickel (0.69 \AA) [26].

The diffraction pattern Rietveld refinement [27] for all samples is executed as shown in Fig. 3, which confirmed that the samples possess two phases: hematite hexagonal phase $\alpha\text{-Fe}_2\text{O}_3$ of the space group $R\text{-}3c$ and cubic spinel phase of the space group $Fd\bar{3}m$. With increasing doping concentration, the volume fraction of the hematite hexagonal phase $\alpha\text{-Fe}_2\text{O}_3$ declined until reached to sample $x = 1$, the hexagonal phase was disappeared. The cubic spinel phase lattice parameter values were computed using the FULL-PROF Program (Le Bail fit) and are presented in Table 1. It is evidently that the lattice constant

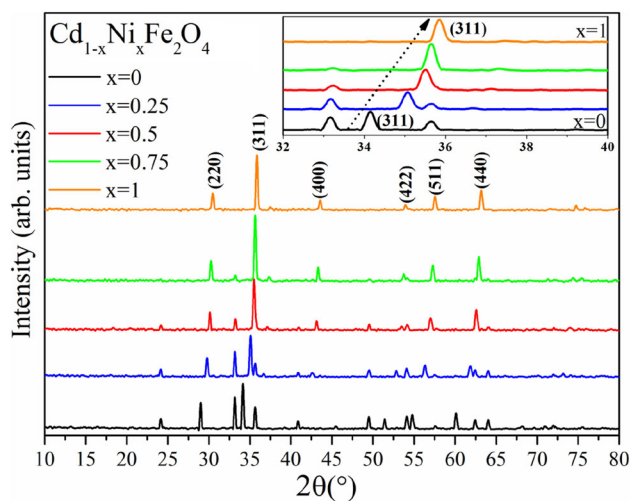


Fig. 2 X-ray diffraction patterns for the prepared samples $\text{Cd}_{1-x}\text{Ni}_x\text{Fe}_2\text{O}_4$. The inset shows remarkable shift of the main peak (311) belonging to cubic spinel ferrite phase towards higher degree (2θ) with increasing Ni content

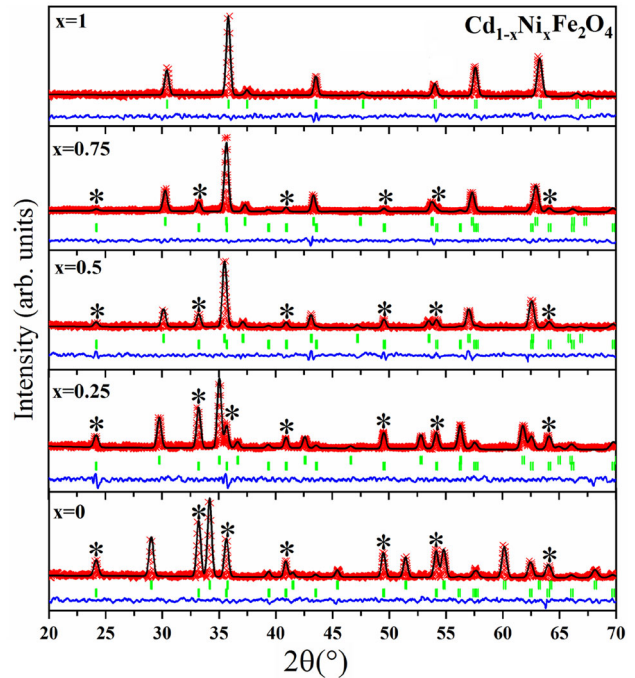


Fig. 3 Observed (symbols) and calculated (line) patterns for all samples. Vertical bars indicate positions of Bragg reflection for the existing phases. The difference between calculated and observed intensities is shown in the bottom. The peaks associated with impurity hematite hexagonal phase $\alpha\text{-Fe}_2\text{O}_3$ are marked with asterisks

decreases with increase in the amount of Ni content. The decreasing of lattice parameters with increasing Ni content can be described on the basis of ionic radii of the impurity ions. The noticeable difference in ionic radii between Cd^{2+} (0.97) and Ni^{2+} (0.69 \AA) might be the major reason for this.

The peak size and strain broadening are additive components of a Bragg peak's total integral width. The separation of size and strain broadening in Williamson and Hall's analysis were based on the distinct angle (θ) dependence of both phenomena [28, 29]. In this work, we use Williamson–Hall formula to calculate the induced strain in the nanocrystals due to lattice imperfection and distortion. The $\text{Fe}_2\text{Cd}_{1-x}\text{Ni}_x\text{O}_4$ samples' crystallite size and lattice strain have been estimated by using the uniform deformation model (UDM) that is presented by Eq. (1). The Williamson–Hall equation for determining the mean crystallite size and lattice strain is shown in Eq. (1) as follows [30]:

$$\beta_{hkl} \cos\theta = \frac{K \cdot \lambda}{D} + 4\epsilon \sin\theta \tag{1}$$

Table 1 Lattice parameter, particle size, lattice strain, theoretical density and hopping lengths L_A and L_B of prepared samples $Cd_{1-x}Ni_xFe_2O_4$

Content	a (Å)	D (nm)	ε	ρ (gm/cm ³)	L_A (Å) ^o	L_B (Å) ^o
$x = 0$	8.6835	61.25	0.014	5.8452	3.760	3.070
$x = 0.25$	8.4903	62.95	0.026	5.9619	3.676	3.001
$x = 0.5$	8.3903	64.19	0.031	5.8754	3.633	2.966
$x = 0.75$	8.3503	79.25	0.045	5.6540	3.615	2.952
$x = 1$	8.3124	80.11	0.054	5.4211	3.599	2.938

where D is the particle size (nm), λ is the wavelength, K is a constant (0.9), β_{hkl} is the peak width at half-maximum intensity, ε is the lattice strain, and θ is the peak position. By plotting $2\sin\theta$ in the x -direction and $\beta_{hkl} \cos\theta$ in the y -direction, which is a linear fit as illustrated in Fig. 4, the crystallite size and lattice strain can be estimated. The size of the nanocrystals is determined by the intercept on the y -axis, while the slope of the plot indicates the average strain induced in the particles. Table 1 revealed that the particle size and lattice strain increase with increasing of Ni content (x).

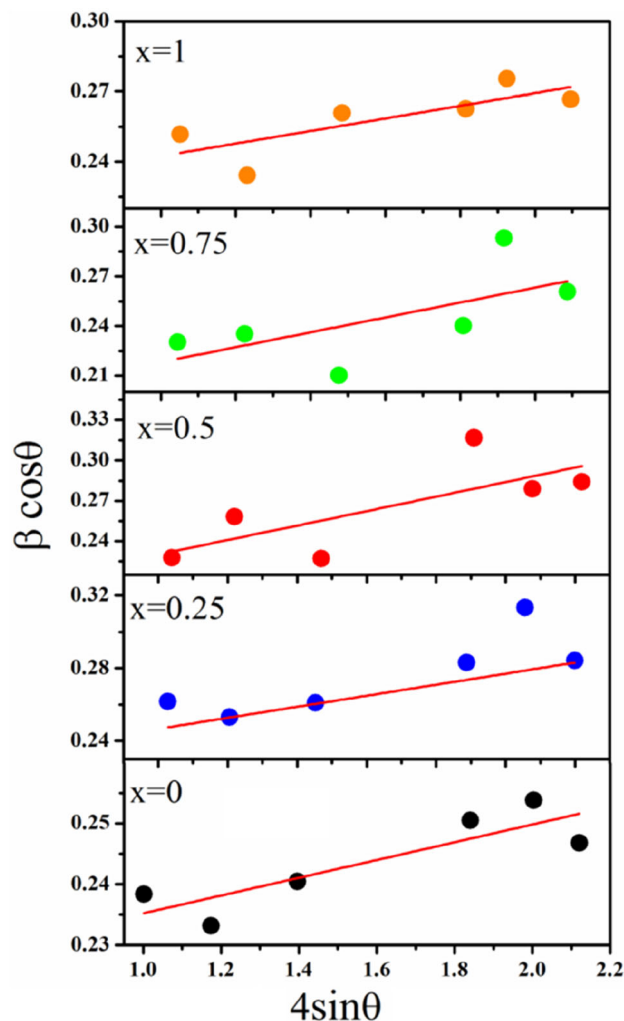
The theoretical density ρ_x of $Cd_{1-x}Ni_xFe_2O_4$ samples was calculated using the relation [31]:

$$\rho_x = \frac{8M}{N_A a^3}, \quad (2)$$

where M is molecular weight of sample, N_A is Avogadro's number, and a is the lattice constant. Table 1 shows that theoretical density ρ_x values $Cd_{1-x}Ni_xFe_2O_4$ samples with increasing Ni content, the convergence in the density values with increasing substitution ratio is due to the convergence in the densities between the Ni (8.9 gm/cm³) and Cd (8.7 gm/cm³).

Using the lattice constant values, hopping lengths L_A (the distance between magnetic ions in A-site "Tetrahedral") and L_B (the distance between magnetic ions in B-site "Octahedral") were calculated as listed in Table 1. L_A and L_B tend to decrease along with increasing nickel content. This can be recognized with shrinkage of the unit cell caused by decreasing in site radius due to incorporation of smaller Ni^{2+} ions into the octahedral lattices and conversion of larger ions into the tetrahedral lattices. Using relation (3, 4), the distance between magnetic ions (hopping length) in tetrahedral A-sites (L_A) and octahedral B-sites (L_B) was estimated (3, 4) [32]:

$$L_A = \frac{a \times \sqrt{3}}{4}, \quad (3)$$

**Fig. 4** A Williamson–Hall plot of $4\sin\theta$ against $\beta\cos\theta$ calculated from XRD spectra for the prepared samples $Cd_{1-x}Ni_xFe_2O_4$

$$L_B = \frac{a \times \sqrt{2}}{4}. \quad (4)$$

3.2 SEM and EDAX analysis

Scanning electron microscopy was used to study the surface morphological characteristics of the cadmium-nickel ferrite samples (SEM). The most of the

particles have been found to be spherical and agglomerated as shown in Fig. 5a. These agglomerates may have formed as a result of a chemical reaction during the sintering process. The replacement of nickel has a considerable impact on grain size and shape, as can be observed. The SEM images were examined by using Image J software, and it is found that the particle size was clearly increased with the increasing Ni concentration (x). The size variation seen in the samples matches the average crystallite sizes estimated from XRD spectra rather well.

The samples energy-dispersive X-ray spectroscopy (EDAX) spectra revealed just the emission peaks of

their constituent elements, revealing no additional impurities as shown in Fig. 5b. The elemental percentages were found to be extremely well coordinated with the calculated weight percentage (wt%) of all elements (i.e., Fe, Cd, Ni, and O) according to stoichiometry using EDAX spectra as listed in Table 2.

3.3 FTIR analysis

The Fourier transform infrared spectroscopy (FTIR) is an effective spectroscopic method for estimating cubic spinel phase synthesis and investigating the

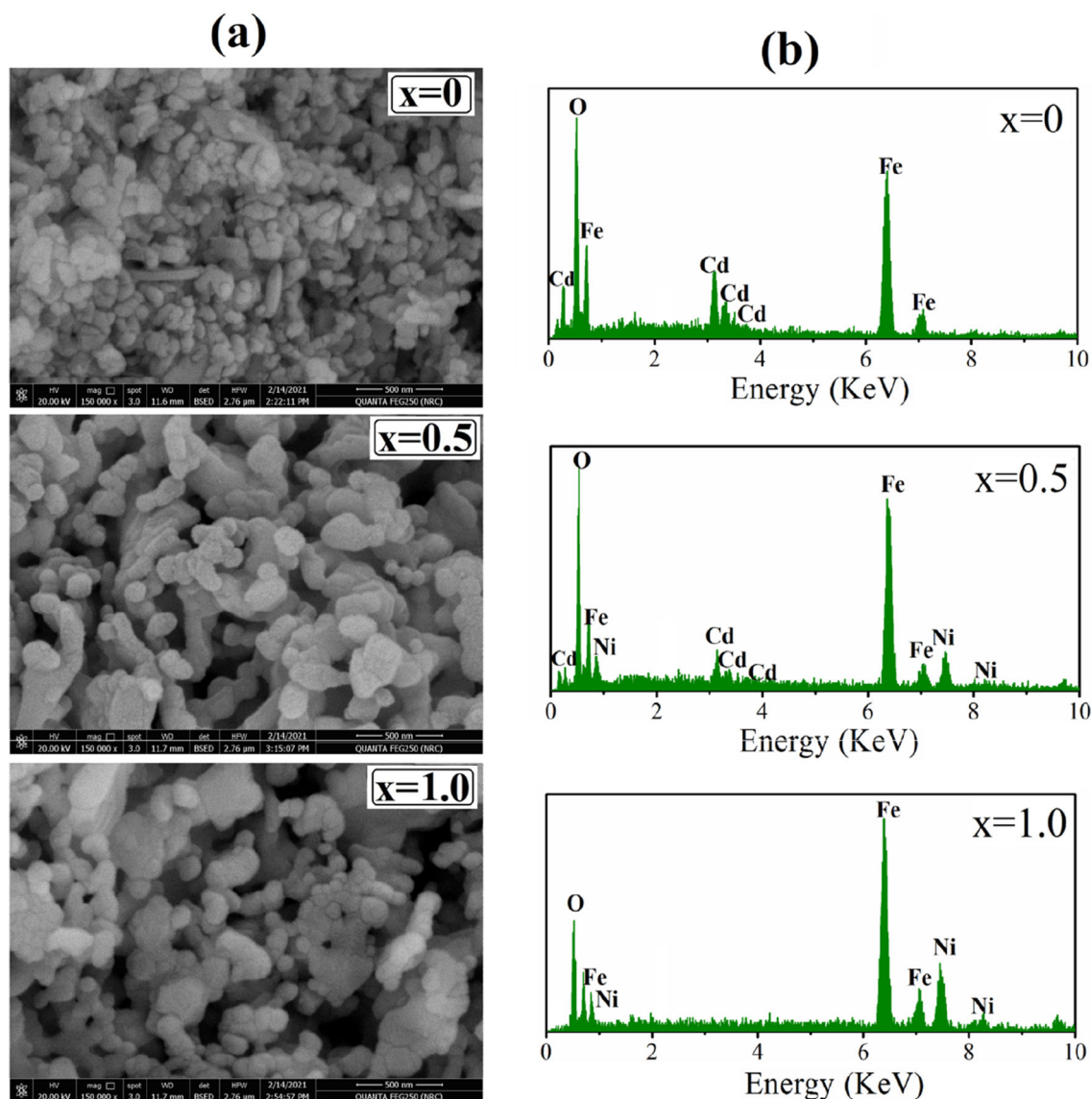
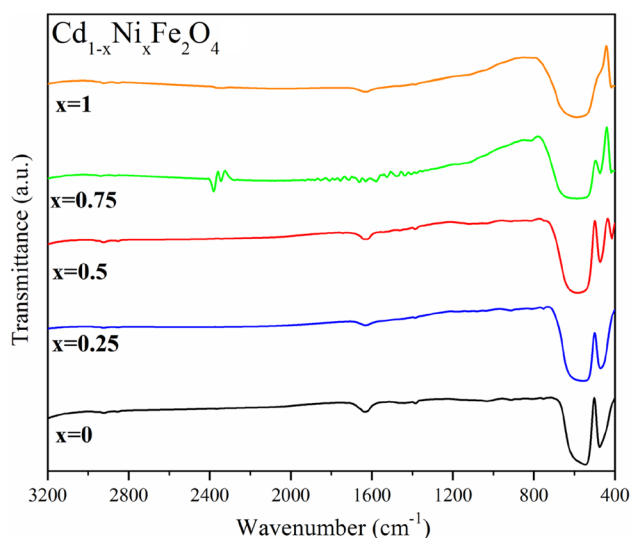


Fig. 5 **a** Scanning electron microphotograph for the samples CdFe_2O_4 ($x = 0$), $\text{Cd}_{0.5}\text{Ni}_{0.5}\text{Fe}_2\text{O}_4$ ($x = 0.5$) and NiFe_2O_4 ($x = 1.0$) spinel ferrite. **b** EDAX spectrum of the $x = 0$, 0.5 and $x = 1.0$ samples

Table 2 EDX analysis of $\text{Cd}_{1-x}\text{Ni}_x\text{Fe}_2\text{O}_4$ ($x = 0, 0.5$ and 1.0) samples

Sample	Element	wt%
$x = 0$	Fe	57.55
	Cd	11.03
	O	31.42
$x = 0.5$	Fe	60.10
	Cd	3.54
	O	20.75
	Ni	15.62
$x = 1$	Fe	62.96
	O	10.03
	Ni	27.01

different functional groups present in materials. FTIR spectrum was measured in the wave number range of $400\text{--}4000\text{ cm}^{-1}$ as exposed in Fig. 6. Metal–oxygen bond peaks at $559\text{--}588\text{ cm}^{-1}$ and $471\text{--}477\text{ cm}^{-1}$ correspond to physical characteristics of ferrites. Consistent with Waldron [33], these peaks are related to the stretching vibrations of metal ion and oxygen bond (M–O) complex, bands in the range $559\text{--}588\text{ cm}^{-1}$ are assigned to tetrahedral sites (A) (ν_t), and $471\text{--}477\text{ cm}^{-1}$ are assigned to octahedral sites (B) (ν_o). Table 3 shows the change in vibrational frequencies at A (ν_t) and B (ν_o) sites as Ni concentration increases. It is important to note that (ν_t) is greater than (ν_o) due to more $\text{Fe}^{3+}\text{--O}^{2-}$ overlapping at A-sites than at B-sites. The position of these two absorption bands is determined by the difference in $\text{Fe}^{3+}\text{--O}^{2-}$ distances for A and B sublattices. Furthermore, the increase in (ν_t) values and decrease in (ν_o)

**Fig. 6** FTIR spectra for the prepared samples $\text{Cd}_{1-x}\text{Ni}_x\text{Fe}_2\text{O}_4$ spinel ferrite

with an increase in Ni^{2+} ion substitution can be ascribed to nonmagnetic divalent Cd^{2+} ions preferring to occupy the tetrahedral sites, forcing Fe and Ni ions to occupy the octahedral sites. According to the fact that Fe^{3+} and Ni^{2+} have a lower ionic radius than Cd^{2+} , causing a decrease in Fe–O bond length and, as a result, a shift in (ν_t) towards higher energy and (ν_o) towards lower energy, this confirms the results discussed in the X-ray diffraction.

By substituting the values of vibrational frequencies (ν_t) and (ν_o) into the following Eq. (5), the force constants of ions corresponding to A-sites (K_T) and B-sites (K_O) may be calculated [34]:

$$K = 4\pi^2 C^2 \nu^2 m, \quad (5)$$

where c is the light speed ($3 \times 10^{10}\text{ cm/s}$), ν is the vibrational frequency at A and B sites, and m is the reduced mass of Fe^{3+} and O^{2-} ($2.601 \times 10^{-23}\text{ g}$). Table 3 presents the values of force constants (K_T) and (K_O); it is important to note that (K_T) values increase while (K_O) values decrease with an increase in Ni content. The increasing of (K_T) and decreasing of (K_O) confirm that nonmagnetic divalent Cd^{2+} ions with higher ionic radius are preferred to occupy the tetrahedral sites, forcing Fe and Ni ions with lower ionic radius to occupy the octahedral sites.

The deconvolution of absorption spectra in the $400\text{--}800\text{ cm}^{-1}$ range is shown in Fig. 7. The peak at 452 cm^{-1} which marked with asterisk is assigned to $\alpha\text{-Fe}_2\text{O}_3$ impurity phase [35, 36]. As can be seen, increasing Ni concentration (x) reduces the intensity of $\alpha\text{-Fe}_2\text{O}_3$ peak which eventually vanishes for $x = 1.0$ sample (Fe_2NiO_4). In addition, the deconvolution of absorption spectra show the shift of vibrational frequencies at A (ν_t) and B (ν_o) sites as Ni concentration increases; this is owing to the fact that Fe^{3+} and Ni^{2+} have a smaller ionic radius than Cd^{2+} , resulting in a decrease in Fe–O bond length.

3.4 Magnetic properties

Hysteresis loops of spinel ferrites samples $\text{Cd}_{1-x}\text{Ni}_x\text{Fe}_2\text{O}_4$ estimated in $\pm 20\text{ kOe}$ field ranges in room temperature are shown in Fig. 8. Normal (S)-shaped curves were detected for all compositions, which display their ferromagnetic character and the magnetic properties were improved by increasing the Ni content. The saturation magnetization (M_s), remanence magnetization (M_r), coercivity (H_c), and the magnetic moment (μ_B) were estimated. It is obvious

Table 3 Variations of tetrahedral (ν_t) and octahedral (ν_o) stretching vibrations and force constants k_t and k_o of $\text{Cd}_{1-x}\text{Ni}_x\text{Fe}_2\text{O}_4$ spinel ferrite nanoparticle samples

x	$\nu_t \text{ cm}^{-1}$	$\nu_o \text{ cm}^{-1}$	$k_t \text{ (Dyne/cm}^{-1}) \times 10^{-5}$	$k_o \text{ (Dyne/cm}^{-1}) \times 10^{-5}$
0.0	559	477	2.8848	2.1006
0.25	558	475	2.8745	2.0830
0.5	570	473	2.9995	2.0655
0.75	584	472	3.1486	2.0568
1.0	588	471	3.1919	2.0481

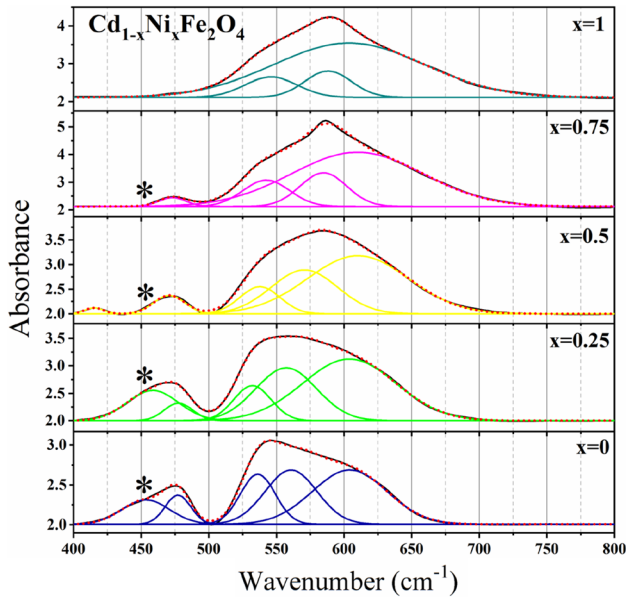


Fig. 7 FTIR deconvolution of absorption spectra in the 400–800 cm^{-1} range

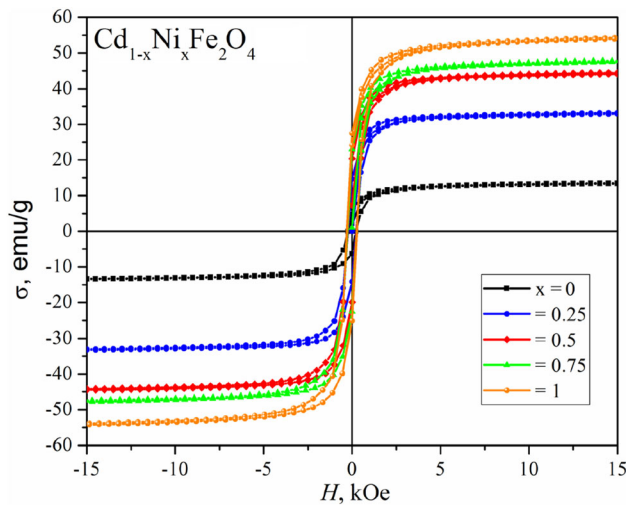


Fig. 8 Room-temperature hysteresis loops for spinel ferrites samples $\text{Cd}_{1-x}\text{Ni}_x\text{Fe}_2\text{O}_4$ obtained in ± 20 kOe field ranges

that magnetic parameters of $\text{Cd}_{1-x}\text{Ni}_x\text{Fe}_2\text{O}_4$ samples increase as a function of Ni content which is related with linkage between (A) and (B) sites as shown in

Fig. 9 and listed in Table 4. The M_s value of undoped Fe_2CdO_4 is 13.45 emu/g, and this value was increased by increasing Ni substitution ratio to 54.352 emu/g for the sample NiFe_2O_4 (pure nickel). It may be as a result of the replacement of diamagnetic Cd^{2+} ions ($0 \mu_B$) by magnetic Ni^{2+} ions ($2 \mu_B$) [37]. The addition of soft magnetic Ni^{2+} ions improves magneto-crystalline anisotropy, allowing samples to maintain magnetic ordering and exhibit soft ferromagnetic behavior.

Using the following relationship (6), the magnetic moment per formula unit in Bohr magneton (B) was computed [38, 39]:

$$\mu_B = \frac{M_s \times M_w}{5585}, \tag{6}$$

where M_s is the saturation magnetization and M_w is the molecular weight of the sample. Table 4 reveals the increasing of magnetic moment in Bohr magneton (μ_B) with increasing Ni content. The improvement of magnetic parameters is because the Cd^{2+} ion strongly occupies the tetrahedral A-site [40, 41]; however, Ni^{2+} ion occupies the octahedral B-site [42] and Fe^{3+} ions occupy both tetrahedral and octahedral sites. According to Nell’s two sublattice

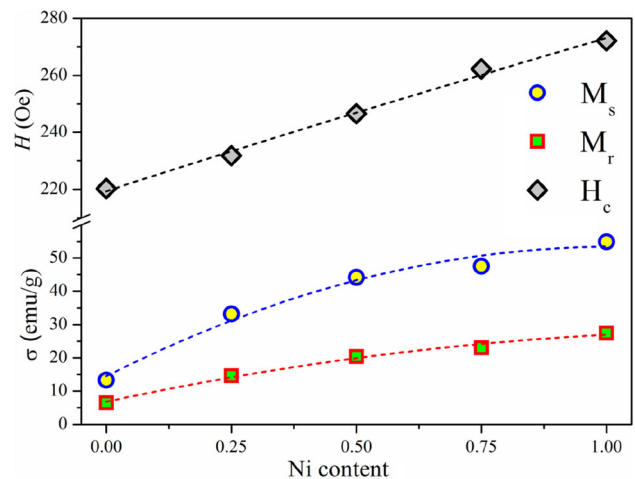


Fig. 9 Dependence of M_s , M_r , and H_c on Ni content for spinel ferrites samples $\text{Cd}_{1-x}\text{Ni}_x\text{Fe}_2\text{O}_4$

Table 4 Magnetic parameters of $\text{Cd}_{1-x}\text{Ni}_x\text{Fe}_2\text{O}_4$ spinel ferrite nanoparticle samples

x	M_s (emu/g)	M_r (emu/g)	H_c (Oe)	M_r/M_s	μ_B (η_B)
0	13.31	6.44	220.25	0.484	0.687
0.25	33.22	14.63	231.76	0.440	1.634
0.5	44.15	20.39	246.56	0.462	2.065
0.75	47.53	23.04	262.20	0.485	2.109
1.00	54.92	27.45	272.07	0.499	2.305

model [43], the addition of magnetic divalent ions (Ni^{2+} ions) in ferrites minimizes the amount of Cd^{2+} ions and increases the amount of Fe^{3+} ions at the A-site, which is responsible for the increase in saturation magnetization and magnetic moment. The occupancy of Ni^{2+} ion at octahedral site (B-site) successively replaces Fe^{3+} ions from B-site and migrates equal amount of Fe^{3+} ions to A-site. As a result, magnetic moment of B-site decreases with increasing Ni^{2+} ion content and the magnetic moment of the A-site sublattice increases due to increasing amount of Fe^{+2} ions. Moreover, the enhanced super-exchange interaction inside the inter-sublattice (A–B) was regarded as the cause of the observed increase in saturation magnetization (M_s), which was compatible with the collinear two sublattice model [44].

3.5 Dielectric properties

The dielectric and electrical properties of the samples $\text{Cd}_{1-x}\text{Ni}_x\text{Fe}_2\text{O}_4$ with $x = 0, 0.25, 0.5, 0.75,$ and 1 depend on the microstructure and synthesis process employed for fabrication are investigated over the considered frequency range. Figure 10 represents the typical dielectric spectra of $\text{Fe}_2\text{Cd}_{1-x}\text{Ni}_x\text{O}_4$ nanoparticle samples as prepared in comparison with that sintered at 950°C . The permittivity, ϵ' , reflects a superposition polarization of the dipoles created from the charge transfer between the divalent and trivalent cations within the spinel structure and the influence of charge carriers' transport. Spinel ferrite's dielectric spectra reveal valuable information about the behavior of localized electric charge carriers and the polarization process in ferrites.

As evident from Fig. 10, the permittivity, ϵ' , shows less dependent (as prepared) or even independent (sintered @ 950°C) behavior as a function of frequency

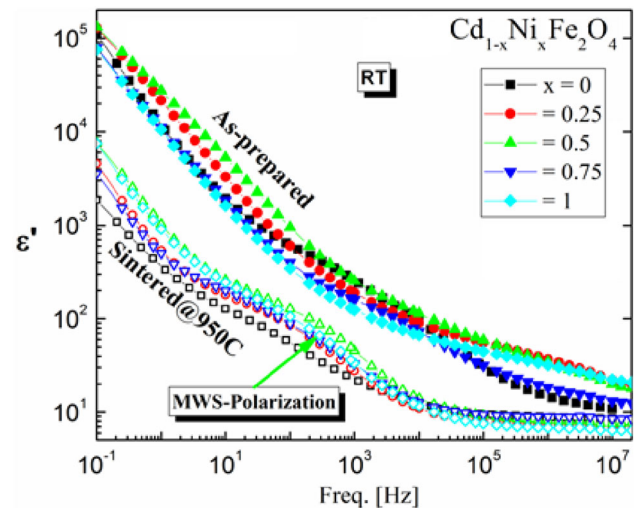


Fig. 10 Permittivity (ϵ') as a function of frequency for all compositions under investigations, $\text{Cd}_{1-x}\text{Ni}_x\text{Fe}_2\text{O}_4$ with $x = (0, 0.25, 0.5, 0.75, 1)$ as-prepared closed symbols and sintered at 950°C (open symbols)

at the higher range of frequency till about 100 kHz. In fact, this is not a surprise at all according to the fact that alterations of all kinds of polarizations lag behind the frequency of the applied field at such higher range. This behavior of ϵ' was found for all investigated compositions and agrees well with that found recently and discussed in detail [24, 45]. During the sintering process, grain boundaries are produced. The layered structure of ferrites can be understood as a result of direct.

Figure 10 shows the intermediate frequency range, a bend-like behavior when the samples are sintered at 950°C . This effect of interfacial polarization (usually called Maxwell–Wagner–Sillars polarization) is originated from the net of micro-capacitors [46]. This phenomenon disappears in case of as-prepared samples at all Ni content. This confirmed the decrease of grain boundaries development and, hence, the absence of the MWS polarization in the case of as-prepared samples. With increase in frequency, role of grain boundaries starts decreasing while that of grains starts increasing, which has resulted in more variation in ϵ' with frequency up to 100 Hz [47]. With higher frequency, the role of grain boundaries becomes less important while the role of grains becomes more important, which has resulted in increasing variance of ϵ' with frequency up to 100 Hz [48].

Conductivity difference between grains and grain boundaries leads to the accumulation of charge

carriers at boundaries, which leads to generation of space charge polarization. As a result, net polarization increases, and hence, higher values of ϵ' are obtained at lower frequencies [49].

The dielectric loss tangent, $\tan \delta$, or the dissipation factor, D , characterizes the rate of energy loss (energy dissipation) in dielectric materials. It is simply the ratio of the dielectric loss, ϵ'' , and the permittivity, ϵ' , as follows in Eq. (7):

$$\tan \delta = \frac{\epsilon''}{\epsilon'}. \tag{7}$$

The values of $\tan \delta$ with respect to frequency for the investigated compositions, sintered at 950 °C, are depicted in Fig. 11. In addition to the dynamic peak relaxation of the interfacial polarization at the intermediate frequencies, there is a higher intensity peak at lower frequencies (slower dynamic) that characterizes the hopping mechanism of the charge carriers' transport. In other words, the peak of slower dynamic of the hopping mechanism in the figure can be attributed to the coincidence of the applied electric field frequency and the hopping frequency of charge carriers. This behavior is observed when the frequency of the applied electric field is smaller than or comparable with the frequency of hopping of charge carriers between Fe^{2+} and Fe^{3+} ions. At higher frequencies, hopping electrons as well as the alteration of MWS polarization do not follow the electric field anymore, and hence, $\tan \delta$ decreases and became stable.

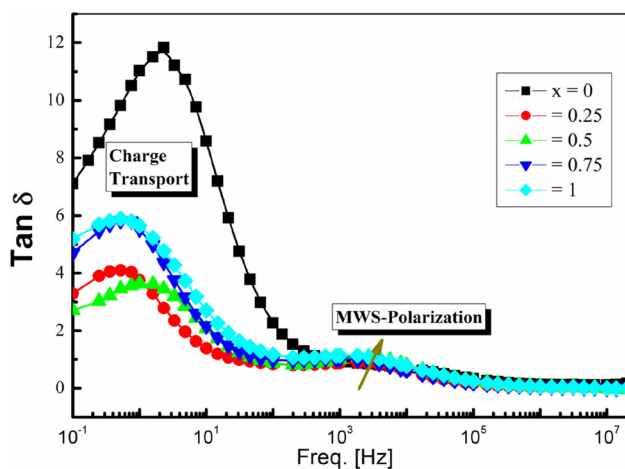


Fig. 11 Dielectric loss tangent, $\tan \delta$ as a function of frequency for all compositions under investigations

The real, M' , and imaginary, M'' , parts of the complex electric modulus can be estimated from those of the complex permittivity by using Eqs. (8, 9);

$$M' = \frac{\epsilon'}{(\epsilon'^2 + \epsilon''^2)}, \tag{8}$$

$$M'' = \frac{\epsilon''}{(\epsilon'^2 + \epsilon''^2)}. \tag{9}$$

The electric modulus calculation helps resolve the relaxation process. Figure 12 shows the Nyquist plot, $M''(M')$ for the samples under investigations. One semi-circular arc (taking in mind the scaling of the plot) corresponds to the relaxation because the grain boundary contribution is shown. Close inspection of the figure shows a shoulder-like behavior at lower range of M' (i.e., at higher frequency range). The Nyquist plot of the complex electric modulus, $M^* = M' + M''$, typically provides accurate information about the conduction mechanism from grain or grain boundaries. The shoulder at higher frequencies signify the resistance of grain only; however, the arc covered the most range of frequencies that characterize the resistance sum of grain and grain boundary [50]. Figure 13 shows the real part of complex conductivity, σ' , as depicted against frequency for the five compositions under investigations as prepared. Two different trends are clearly shown in the figure. At higher frequency range, the ac conductivity increases gradually with increasing frequency. This increase of σ' is supposed to be linearly on the log–log plot and follows the power law (that is, $= k^n$, where k

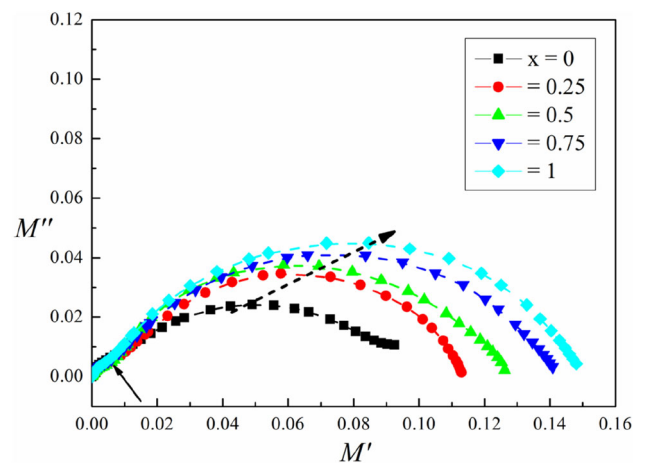


Fig. 12 The imaginary part of complex electric modulus as illustrated graphically against its real part (Nyquist plot) of the investigated samples as indicated

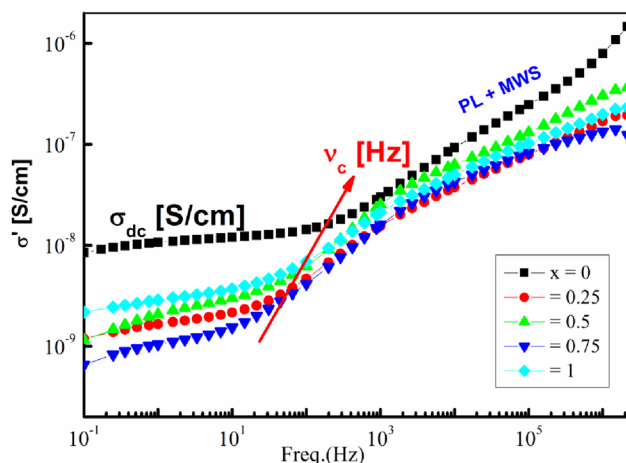


Fig. 13 Real part of the complex conductivity, σ' , vs. frequency for all compositions under investigations

and n are constants and ω is the radial frequency). This is usually explained according to the fact that, the electrical conductivity in ferrites is originated mainly from hopping of electrons between ions of same element existing in the different valence states. The increase in Ni^{+2} concentrations replaces more Fe^{+2} ions and, hence, reducing the conductivity. Upon the application of ac field, the electron hopping increases, in that way enhances the ac conductivity. However, the deviation from linearity reflects that the accompanying of interfacial polarization (usually called Maxwell–Wagner–Sillier polarization) comes from the accumulation of charge carriers at the interphases. The electrical response of the system is influenced by charges migrating under the effect of an applied ac field [51]. At some characteristic frequency (ν_c), ac conductivity tends to be less dependent or even independent on the frequency of the applied external field at lower frequency range. The ac conductivity, σ_{ac} here is considered to be dc conductivity, σ_{dc} .

The ac conductivity can be signified by the next relation (10).

$$\sigma(\omega) = \sigma_{dc} + \sigma_{ac}(\omega) \quad (10)$$

There are two components to this equation: the first component is a frequency-independent part called dc conductivity, σ_{dc} , which is due to band conduction, and the second term is a frequency-dependent part called ac conductivity, σ_{ac} , which is due to electron hopping at the B-site. One has to notice that the increase of σ_{dc} is accompanied by gradual increase of ν_c . Both parameters are linearly related to each other

according to the empirical Barton–Nakajima–Nami-kawa (BNN) relationship $\sigma_{dc} \sim \nu_c$ [52–55]. One can conclude that the increase of the characteristic frequency leads to increase of the conductivity. Taking into consideration, the frequency is the reciprocal of time. In other words, the shorter the time is, the higher the conductivity. This confirms that the time here is nothing rather than the hopping time of the ion.

4 Conclusion

By using the flash auto-combustion method, Ni-substituted CdFeO spinel ferrites were successfully synthesized. The crystal structure, dielectric, and magnetic characteristics of $\text{Cd}_{1-x}\text{Ni}_x\text{Fe}_2\text{O}_4$ spinel nano-ferrites samples were demonstrated to be significantly influenced by Ni substitution. X-ray diffraction study confirmed that the investigated samples have the cubic phase spinel ferrite with space group $\text{Fd}\bar{3}\text{m}$ and the lattice parameters decrease with increasing Ni concentration. As well as the particle size was clearly increased with the increasing Ni concentration. FTIR analysis revealed two fundamental tetrahedral and octahedral stretching vibrations of metal–oxygen bond peaks at $559\text{--}588\text{ cm}^{-1}$ and at $471\text{--}477\text{ cm}^{-1}$ approving spinel structure of prepared ferrites. The increasing in vibrational frequencies at A (ν_t) and decreasing in vibrational frequencies B (ν_o) sites have been estimated. Magnetic measurements show an improvement in all characteristics such as saturation magnetization (M_s), remanence magnetization (M_r), coercivity (H_s), and magnetic moment (μ_B) by increasing Ni substitution content. The interfacial polarization in case of the sintered compositions at $950\text{ }^\circ\text{C}$ reflects the development of micro-capacitors net originated from the well-conducting grains separated by thin layer of poorly conducting grain boundaries. This effect is remarkably reduced in case of the as-prepared samples. The increase in Ni^{+2} concentrations replaces more Fe^{+2} ions and, hence, reducing the conductivity.

Author contributions

MHN, ASA, and AAE-H performed all the experimental work (sample preparation and its characterization) and prepared manuscript. GMT performed

the dielectric measurements and its discussion. MME and LMSE-D helped significantly in the explanation of experimental results.

Data availability

The data that support the findings of this study are available from the corresponding author upon reasonable request.

Declarations

Conflict of interest There is no conflict of interest among the contributing authors.

References

1. AT Ngo MP Pileni 2001 Assemblies of ferrite nanocrystals: partial orientation of the easy magnetic axes *J. Phys. Chem. B* 105 1 53 58
2. A Sutka KA Gross 2016 Spinel ferrite oxide semiconductor gas sensors *Sens. Actuators B* 222 95
3. MA Hakim SK Nath SS Sikder KH Maria 2013 Cation distribution and electromagnetic properties of spinel type Ni–Cd ferrites *J. Phys. Chem. Solids* 74 9 1316
4. SP Yadav KY Rajpure R Urkude YM Hunge Kamlesh V Chandekar 2021 Dielectric and magneto-electric behavior of (x) $\text{Co}_{0.8}\text{Mn}_{0.2}\text{Fe}_2\text{O}_4$ and (1-x) $\text{PbZr}_{0.52}\text{Ti}_{0.48}\text{O}_3$ composites *Physica B* 617 413118
5. AA Yadav YM Hunge S Liu SB Kulkarni 2019 Ultrasound assisted growth of NiCo_2O_4 @carbon cloth for high energy storage device application *Ultrason. Sonochem.* 56 290 296
6. RK Sharma R Ghose 2015 Synthesis and characterization of nanocrystalline zinc ferrite spinel powders by homogeneous precipitation method *Ceram Int.* 41 14684 14691
7. HK Dubey C Verma US Rai A Kumar P Lahiri 2019 Synthesis characterization and properties of nickel-based zinc ferrite nanoparticles *Ind. J. Chem. A* 58 454 458
8. PB Belavi GN Chavan LR Naik R Somashekar RK Kotnala 2012 Structural, electrical and magnetic properties of cadmium substituted nickel–copper ferrites *Mater. Chem. Phys.* 132 138 144
9. C Cheng 2008 Long-range antiferromagnetic interactions in ZnFe_2O_4 and CdFe_2O_4 : density functional theory calculations *Phys. Rev. B* 78 132403 132406
10. D Ahmad N Mehboob A Zaman N Ahmed K Ahmed M Mushtaq K Althubeiti A Ali F Sultana K Bashir 2021 Synthesis and characterization of Ce^{3+} -Doped $\text{Ni}_{0.5}\text{Cd}_{0.5}\text{Fe}_2\text{O}_4$ nanoparticles by sol-gel auto-combustion method *Coatings* 11 1156
11. B.H. Devmunde, A.V. Raut, S.D. Birajdar, S.J. Shukla, D.R. Shengule, K.M. Jadhav, Structural, electrical, dielectric, and magnetic properties of Cd^{2+} substituted nickel ferrite nanoparticles. *J. Nanoparticles* Article ID 4709687, (2016).
12. KM Badoo 2011 Microstructural and Mossbauer properties of low temperature synthesized Ni–Cd–Al ferrite nanoparticles *Nanoscale Res. Lett.* 6 499 505
13. GN Chavan PB Belavi LR Naik BK Bammannavar KP Ramesh S Kumar 2013 Electrical and magnetic properties of nickel substituted cadmium ferrites *Int. J. Sci. Technol. Res.* 2 12
14. VG Panicker RV Upadhyay SN Rao RG Kulkarni 1984 Noncolinear spin structure in Ni–Cd ferrite system *J. Mater. Sci. Lett.* 3 385 387
15. SK Nath KH Maria S Noor SS Sikder SM Hoque MA Hakim 2012 Magnetic ordering in Ni–Cd ferrite *J. Magn. Magn. Mater.* 324 13 2116 2120
16. JZ Msomi 2013 Structural and magnetic changes induced by high energy ball milling of CdFe_2O_4 *J. Magn. Magn. Mater.* 336 61 65
17. E Wolska W Wolski J Kaczmarek E Riedel D Prick 1992 Defect structures in cadmium-nickel ferrites *Solid State Ionics* 51 3–4 231 237
18. R Desai RV Mehta RV Upadhyay A Gupta A Praneet KV Rao 2007 “Bulk magnetic properties of CdFe_2O_4 in nano-regime *Bull. Mater. Sci.* 3 197 203
19. M Yokoyama E Ohta T Sato T Sato 1998 Magnetic properties of ultrafine particles and bulk material of cadmium ferrite *J. Magn. Magn. Mater.* 183 1–2 173 180
20. V Vasanthi A Shanmugavani C Sanjeeviraja R KalaiSelvan 2012 Microwave assisted combustion synthesis of CdFe_2O_4 : magnetic and electrical properties *J. Magn. Magn. Mater.* 324 13 2100 2017
21. PK Nayak 2008 Synthesis and characterization of cadmium ferrite *Mater. Chem. Phys.* 112 1 24 26
22. A Sutka G Mezinskis 2012 Sol-gel auto-combustion synthesis of spinel type ferrite nanomaterials *Front. Mater. Sci.* 6 2 128 141
23. M Airimioaei CE Ciomaga N Apostolescu L Leontie AR Iordan L Mitoseriu MN Palamaru 2011 Synthesis and functional properties of the $\text{Ni}_{1-x}\text{Mn}_x\text{Fe}_2\text{O}_4$ ferrites *J. Alloy. Compd.* 509 31 8065 8072
24. A.S. Abouhaswa, M.H. Badr, M.H. Nasr, M.M. Elkholy, L.M.S. El-Deen, G.M. Turky, M. Moustafa, A.A. EL-Hamalawy, Investigation of crystal structure, electrical and magnetic properties of spinel Mn–Cd ferrite nanoparticles. *J. Inorg. Organomet. Polym. Mater.* <https://doi.org/10.1007/s10904-021-02116-9> (2021).

25. M Sinha SK Pradhan 2010 Synthesis of nanocrystalline Cd–Zn ferrite by ball milling and its stability at elevated temperatures *J. Alloy Compd.* 489 91 98
26. RD Shannon 1976 Revised effective ionic radii and systematic studies of interatomic distances in halides and chalcogenides *Acta Crystallogr. Sect. A* <https://doi.org/10.1107/S0567739476001551>
27. HM Rietveld 1969 A profile refinement method for nuclear and magnetic structures *J. Appl. Cryst.* 2 65 71
28. VK Kumar D Paramesh P Venkat Reddy 2015 Effect of aluminium doping on structural and magnetic properties of Ni–Zn ferrite nanoparticles *World J. Nano Sci. Eng.* 5 68 77
29. AB Kulkarni SN Mathad 2018 Effect of sintering temperature on structural properties of Cd doped Co–Zn ferrite *J. Nano-Electron. Phys.* 10 1 01001
30. VD Mote Y Purushotham BN Dole 2012 Williamson–Hall analysis in estimation of lattice strain in nanometer-sized ZnO particles *J. Theor. Appl. Phys.* 6 1
31. DV Kurmude RS Barkule AV Raut DR Shengule KM Jadhav 2014 X-ray diffraction and cation distribution studies in zincsubstituted nickel ferrite nanoparticles *J. Supercond. Nov. Magn.* 27 547 553
32. M. Satalkar, S. N. Kane, On the study of structural properties and cation distribution of $Zn_{0.75-x}Ni_xMg_{0.15}Cu_{0.1}Fe_2O_4$ nano ferrite: effect of Ni addition. *J. Phys.* 755, 012050 (2016).
33. RD Waldron 1955 Infrared spectra of ferrites *Phys Rev.* 99 1727 1735
34. L Phor S Chahal V Kumar 2020 Zn^{2+} substituted superparamagnetic $MgFe_2O_4$ spinel-ferrites: Investigations on structural and spin-interactions *Journal of Advanced Ceramics* 9 5 576 587
35. S Suman A Chahal P Kumar 2020 Kumar, Zn Doped α - Fe_2O_3 : An Efficient material for UV driven photocatalysis and electrical conductivity *Curr. Comput. Aided Drug Des.* 10 4 273
36. AT Raghavender N Biliškov Ž Skoko 2011 XRD and IR analysis of nanocrystalline Ni–Zn ferrite synthesized by the sol–gel method *Mater. Lett.* 65 677 680
37. A. Goldman, *Modern Ferrite Technology*, Van Nostrand Reinhold Company, New York, NY, USA
38. H Bahiraei MZ Shoushtari K Gheisari CK Ong 2014 The effect of sintering temperature on the electromagnetic properties of nano-crystalline Mg Cu Zn ferrite prepared by sol-gel auto combustion method *Mater Lett* 32 122 129
39. F Meng X Shang W Zhang Y Zhang 2017 Effect of In^{3+} substitution on structural and magnetic properties of Ni ferrite nanoparticles *Physica B* 504 69 73
40. SA Patil VC Mahajan AK Gatge SD Lotake 1998 Structure and magnetic properties of Cd and Ti/Si substituted cobalt ferrites *Mater. Chem. Phys.* 57 86
41. OM Hemedat MM Barakat 2001 Effect of hopping rate and jump length of hopping electrons on the conductivity and dielectric properties of Co–Cd ferrite *J. Magn. Magn. Mater.* 223 127
42. GK Joshi AY Khot SR Savant 1988 Magnetisation, curie temperature and YK angle studies of Cu substituted and non-substituted NiZn mixed ferrites *Solid State Commun.* 65 1593
43. Y Yafet C Kittel 1952 Antiferromagnetic arrangements in ferrites *Phys. Rev.* 87 290
44. R. Tiwari, Manojit De, H.S. Tewari, S.K. Ghoshal, Structural and magnetic properties of tailored $NiFe_2O_4$ nanostructures synthesized using auto-combustion method, *Results in Physics* 16, 1029162, (2020).
45. AM Fayad M Abdel-Baki EM Hamzawy GM Turkey GT El-Bassyouni 2020 Influence of CuO on crystallization and electrical properties of B_2O_3 - Bi_2O_3 - GeO_2 - CaF_2 glass system for optoelectronic application *J. Non-Cryst. Solids* 544 120 185
46. MA El Hiti 1999 Dielectric behaviour in Mg–Zn ferrites *J. Magn. Magn. Mater.* 192 305
47. N El-Mehalawy M Awaad GM Turkey MW Ali-Bik SH Abd El Rahim SM Naga 2021 Self-glazing dielectric ceramic bodies fabricated from egyptian rhyodacite and kaolin *Mater. Chem. Phys.* 270 124785
48. MH Dhaou S Hcini A Mallah ML Bouazizi A Jemni 2017 Structural and complex impedance spectroscopic studies of $Ni_{0.5}Mg_{0.3}Cu_{0.2}Fe_2O_4$ ferrite nanoparticle *Appl. Phys. A* 123 8
49. H Sözeri F Genç B Ünal A Baykal B Aktaş 2016 Magnetic, electrical and microwave properties of Mn–Co substituted $Ni_xZn_{0.8-x}Fe_2O_4$ nanoparticles *J. Alloy Compd.* 660 324 335
50. AK Pradhan PR Mandal K Bera S Saha TK Nath 2017 The effect of Mo doping on the structural and dielectric properties of Co–Zn ferrite *Physica B* 525 1
51. J Parashar VK Saxena J Sharma D Bhatnagar KB Sharma 2015 Dielectric behaviour of $Ni_{0.2}Cu_{0.2}Zn_{0.6}Fe_2O_4$ spinel ferrite *Macromol. Symp.* 357 43
52. J Barton 1966 Dielectric relaxation of some ternary alkali-alkaline earth-silicate glasses *Verres Refract* 20 328 335
53. T. Nakajima, 1971 Annual Report, Conference on Electric Insulation and Dielectric Phenomena (1972).
54. H Namikawa 1975 Characterization of the diffusion process in oxide glasses based on the correlation between electric conduction and dielectric relaxation *J. Non-Cryst. Solids* 18 173 195
55. MA Moussa MH Abdel Rehim GM Turkey 2021 *J. Phys. Chem. Solids* 158 110243

Publisher's Note Springer Nature remains neutral with regard to jurisdictional claims in published maps and institutional affiliations.